

Space–time topology optimization for anisotropic materials in wire and arc additive manufacturing

Wu, Kai; Wang, Weiming; van Keulen, Fred; Wu, Jun

DOI

[10.1016/j.ijmecsci.2024.109712](https://doi.org/10.1016/j.ijmecsci.2024.109712)

Publication date

2024

Document Version

Final published version

Published in

International Journal of Mechanical Sciences

Citation (APA)

Wu, K., Wang, W., van Keulen, F., & Wu, J. (2024). Space–time topology optimization for anisotropic materials in wire and arc additive manufacturing. *International Journal of Mechanical Sciences*, 284, Article 109712. <https://doi.org/10.1016/j.ijmecsci.2024.109712>

Important note

To cite this publication, please use the final published version (if applicable). Please check the document version above.

Copyright

Other than for strictly personal use, it is not permitted to download, forward or distribute the text or part of it, without the consent of the author(s) and/or copyright holder(s), unless the work is under an open content license such as Creative Commons.

Takedown policy

Please contact us and provide details if you believe this document breaches copyrights. We will remove access to the work immediately and investigate your claim.



Contents lists available at ScienceDirect

International Journal of Mechanical Sciences

journal homepage: www.elsevier.com/locate/ijmecsci

Space–time topology optimization for anisotropic materials in wire and arc additive manufacturing

Kai Wu^a, Weiming Wang^b, Fred van Keulen^a, Jun Wu^{c,*}

^a Faculty of Mechanical Engineering, Delft University of Technology, Mekelweg 2, Delft, 2628 CD, The Netherlands

^b Department of Mechanical, Aerospace and Civil Engineering, The University of Manchester, Oxford Road, Manchester, M13 9PL, United Kingdom

^c Faculty of Industrial Design Engineering, Delft University of Technology, Landbergstraat 15, Delft, 2628 CE, The Netherlands

ARTICLE INFO

Keywords:

Topology optimization
Additive manufacturing
Computer-aided manufacturing
Fabrication sequence Planning
Anisotropic material

ABSTRACT

Wire and Arc Additive Manufacturing (WAAM) has great potential for efficiently producing large metallic components. However, like other additive manufacturing techniques, materials processed by WAAM exhibit anisotropic properties. Assuming isotropic material properties in design optimization thus leads to less efficient material utilization. Instead of viewing WAAM-induced material anisotropy as a limitation, we consider it an opportunity to improve structural performance. This requires the integration of process planning into structural design. In this paper, we propose a novel method to utilize material anisotropy to enhance the performance of structures both during fabrication and in their use. Our approach is based on space–time topology optimization, which simultaneously optimizes the structural layout and the fabrication sequence. To model material anisotropy in space–time topology optimization, we derive the material deposition direction from the gradient of the pseudo-time field, which encodes the fabrication sequence. Numerical results demonstrate that leveraging material anisotropy effectively improves the performance of intermediate structures during fabrication as well as the overall structure.

1. Introduction

Topology optimization is essential in structural design for additive manufacturing. By topology optimization, structural design is transformed into an optimization problem of determining the optimal material distribution to maximize structural performance, such as creating lightweight structures with high load-bearing capacity [1,2]. It has been widely applied across engineering disciplines, including aerospace, automotive, civil and biomechanical engineering. Additive manufacturing (AM, also known as 3D printing) fabricates components layer-upon-layer from digital models. In an AM process, the material is added precisely where needed, allowing for complex geometries, customization, and reduced waste compared to traditional manufacturing methods [3]. The design freedom provided by topology optimization complements the manufacturing flexibility of AM, allowing for the creation of components with exceptional performance [4,5]. However, the complex geometries resulting from topology optimization often pose production challenges, even with advanced AM techniques. Consequently, integrating AM constraints into structural design optimization has been a key research area over the past decade. Important issues that have been addressed include overhang limitation [6–8], local overheating [9], support structures [10,11], and residual stresses [12,13]. We

refer to the review articles [14–16] for a comprehensive overview of developments in topology optimization for AM.

Beyond structural design, the manufacturing process itself greatly influences the quality of additively produced components. For example, in wire and arc additive manufacturing (WAAM) [17–19], substantial distortion may occur during fabrication and after cutting off from the build plate. An essential aspect of manufacturing process planning is the fabrication sequence, which dictates the layer-by-layer construction of the structure. In traditional 2.5D printing, where each layer is planar and parallel to each other, the layer-wise sequence is uniquely defined by the orientation of the structure on the build plate. Topology optimization, combined with build orientation optimization for 2.5D printing, has been explored in several studies [20–25]. However, advancements in multi-axis printing using robotic arms, capable of rotational and translational movements, allow for material deposition along non-planar layers [26–29]. This capability expands the solution space for fabrication sequence planning. Optimizing the fabrication sequence can significantly enhance the quality of fabricated components. For instance, it reduces structural distortions caused by high temperature gradients and phase transitions in WAAM [30].

* Corresponding author.

E-mail address: j.wu-1@tudelft.nl (J. Wu).

<https://doi.org/10.1016/j.ijmecsci.2024.109712>

Received 25 May 2024; Received in revised form 30 August 2024; Accepted 7 September 2024

Available online 18 September 2024

0020-7403/© 2024 The Author(s). Published by Elsevier Ltd. This is an open access article under the CC BY license (<http://creativecommons.org/licenses/by/4.0/>).

Fabrication sequences are typically planned after the structure has been designed, leading to insufficient consideration of the manufacturing process during the design phase. This disconnect results in discrepancies between digital designs and their physical counterparts. Recent studies aim to close this gap by integrating manufacturing process planning into structural design optimization [31,32]. Achieving optimal structural performance necessitates a holistic approach that concurrently optimizes both the structural layout and the fabrication sequence [33,34]. Known as space–time topology optimization [33], it introduces a pseudo-time field alongside the pseudo-density field used in conventional topology optimization. The pseudo-time field encodes the fabrication sequence, facilitating the planning of the sequence as the structural layout evolves during optimization. The isolines of the pseudo-time field divide the structural layout into an ordered sequence of curved layers, enabling the analysis of intermediate structures that emerge during the manufacturing process.

Previous implementations of the space–time topology optimization framework have generally assumed isotropic material properties. However, in AM, material properties such as elastic modulus, tensile strength, and yield strength are significantly influenced by the manufacturing process, leading to anisotropic behavior [35–43]. Assuming isotropic material properties in design optimization thus leads to suboptimal performance [44–48]. In WAAM, material anisotropy is particularly prevalent in components fabricated from materials like austenitic stainless steel [49] and Ti-6Al-4V [50], primarily due to rapid and uneven solidification during manufacturing [49]. It is therefore important to take material anisotropy into account when designing for WAAM [51,52].

In this paper, we propose a novel method to utilize material anisotropy to enhance the performance of structures both during fabrication and in their use. By considering the effects of material anisotropy in the concurrent optimization of structural design and process planning, we aim to reduce the gap between digital designs and their physical counterparts, ultimately enhancing the quality of produced components.

The consideration of material anisotropy in structural topology optimization dates back to the 1980s. Early research was driven by the anisotropic properties of laminated and fiber-reinforced composites [53–57]. Pedersen [58,59] established that the optimal orientations of orthotropic materials for maximizing structural stiffness align with the principal stress directions. This foundation led to stress-based methods [28,60–65] where the material reinforcement direction is derived from principal stress directions. For structures subjected to multiple load cases, the arrangement of local material orientation is treated as an optimization problem, with material orientation defined as either a discrete or continuous variable, represented using the polar angle [66,67] or a vector in the Cartesian coordinate system [68,69]. This approach has been integrated with topology optimization to simultaneously optimize structural layout and material orientation [66–70]. However, these methods are not directly applicable to design for additive manufacturing, as they either derive material orientation from stress fields or treat local material orientation as independent optimization variables. The resulting optimized anisotropic material orientation may not be achievable through an AM process.

Recent studies have incorporated material anisotropy in structural optimization for AM, coupling material orientation with structural design based on material deposition toolpaths in AM processes. Level-set-based topology optimization [2] is particularly well-suited for this purpose, where iso-value level set contours are interpreted as deposition toolpaths, with material orientations aligned accordingly [71–74]. While this typically results in toolpaths that are quasi-parallel to the optimized shape's boundary, it does not allow for more complex patterns, such as zig-zag toolpaths. Vibhas et al. [51] proposed a method to optimize structural design for WAAM by integrating material anisotropy, with deposition toolpaths manually derived from the optimized orientation in a post-processing step. Automated extraction of toolpaths from

specialized topology optimization methods has also been explored, such as the phase-field de-homogenization approach [75] and the streamline algorithm [76]. However, it is important to note that in both these methods and others, the toolpaths are static and do not determine the printing order. Our work differs by specifically analyzing the printing order of toolpaths, an investigation made possible through space–time topology optimization [30,33,77].

In space–time topology optimization, the fabrication sequence is represented by a pseudo-time field, and it is optimized concurrently with the pseudo-density field representing the structural layout. To integrate material anisotropy into space–time topology optimization, a differentiable relationship between material anisotropy and the fabrication sequence should be established. In this paper, we will illustrate that the anisotropic material orientation can be implicitly derived from the pseudo-time field. Furthermore, the printing order can also be derived from the pseudo-time field, allowing us to predict its consequence on printing quality. This research demonstrates the feasibility and benefits of incorporating manufacturing-induced material anisotropy in space–time topology optimization.

The remainder of the paper is organized as follows. Section 2 details the mathematical model underlying our method. Section 3 presents a series of numerical examples, validating the effectiveness of the proposed method. Lastly, Section 4 summarizes the key findings and contributions.

2. Method

In this section, we first introduce the parameterization of the structural layout and fabrication sequence, specifically the space–time parameterization using pseudo-density and pseudo-time fields (Section 2.1). Next, we discuss the anisotropic material model, emphasizing the relationship between material anisotropy and the pseudo-time field (Section 2.2). The computational steps involved in space–time topology optimization are detailed in Section 2.3. Finally, Section 2.3.3 presents the mathematical model for space–time topology optimization with anisotropic materials, along with the pseudo-code summarizing the solution process.

2.1. Space–time parameterization

Here we review the parameterization for space–time topology optimization, which forms the foundation of our current work. In space–time optimization, both the structural layout and the corresponding fabrication sequence are optimized concurrently. The structural layout is represented using a pseudo-density field ρ , as in classic density-based topology optimization. Simultaneously, the fabrication sequence is encoded through a pseudo-time field t . For simplicity, the pseudo-density and pseudo-time fields are referred to as density and time fields, respectively. These fields are defined in the domain of the 2D or 3D component.

Applying the same discretization to both density and time fields, each element is assigned two variables, ρ_e and t_e . In a discrete setup, the density ρ_e assumes values of either 0 or 1, where $\rho_e = 0$ indicates void and $\rho_e = 1$ represents solid material. To avoid solving a binary optimization problem, this binary design variable is relaxed, allowing densities to take intermediate values. Correspondingly, the elastic modulus associated with intermediate density values is determined by a commonly used material interpolation model, *i.e.*, SIMP (Solid Isotropic Material with Penalization).

Unlike the intended binary representation of the density field, the time variable t_e assumes continuous values between 0 and 1. A higher time value indicates that an element is to be built later in the manufacturing process. Specifically, a time value of 0 denotes the beginning of manufacturing, while 1 indicates that the element is produced at the very end of the manufacturing process.

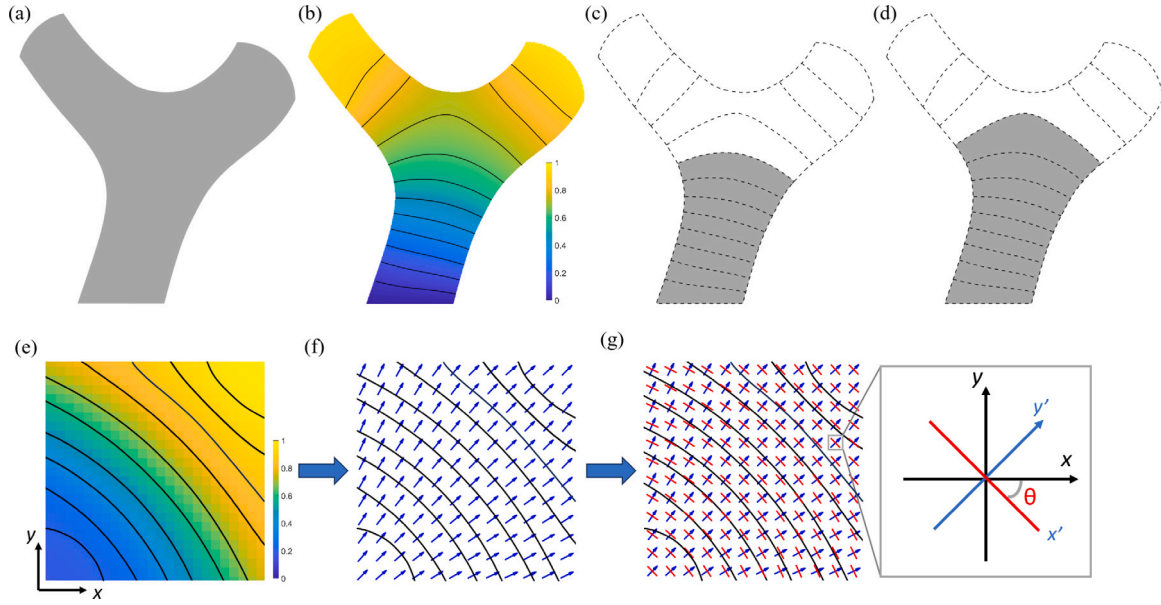


Fig. 1. Illustration of space-time parameterization and the orthogonal relationship between the gradient of the time field and the local material orientation. Top row: (a) A structural layout, represented by a density field. (b) The structure color-coded by a time field, with the isolines partitioning the structure into 12 layers. (c, d) Two successive intermediate structures during fabrication, in which 8 or 9 layers have been produced. Bottom row: (e) The time field in a rectangular domain. (f) The normalized gradient (blue arrow) of the time field. (g) The local material deposition direction (red) is perpendicular to the gradient vector element-wise. The local material orientation is denoted by angle θ .

As illustrated in Fig. 1, from the continuous time field, a series of intermediate structures is derived. Fig. 1(a) shows the structural layout, represented by a density field. Fig. 1(b) visualizes the time field on the structure using a colormap. The isolines of the time field partition the component into a series of layers. The iso-values are $\tau_j = \frac{j}{N}$, $j = 0, 1, \dots, N$, with N being the prescribed number of layers. The elements with a time value belonging to the interval $[\tau_{j-1}, \tau_j]$, $j = 1, \dots, N$, are part of the j th layer. Fig. 1(c) and (d) illustrate the intermediate structure at two consecutive stages during the manufacturing process. The intermediate structure at time τ is composed of elements with a time value equal to or less than τ . Elements with a time value larger than τ have not been produced and thus are assigned a density value of zero,

$$\rho_e^{(\tau)} = \begin{cases} \rho_e, & \text{if } t_e \leq \tau, \\ 0, & \text{otherwise.} \end{cases} \quad (1)$$

To facilitate gradient-based optimization, this conditional equation is approximated using a smoothed Heaviside function,

$$\rho_e^{(\tau)} = \rho_e \tilde{r}_e^{(\tau)}, \quad (2)$$

with

$$\tilde{r}_e^{(\tau)} = 1 - \frac{\tanh(\beta_t \tau) + \tanh(\beta_t (t_e - \tau))}{\tanh(\beta_t \tau) + \tanh(\beta_t (1 - \tau))}. \quad (3)$$

Here, β_t determines the sharpness of the step function. This function converts, in a differentiable manner, a time value smaller than the threshold value τ to 1, and, conversely, a time value larger than τ to 0.

2.2. Material anisotropy

From the time field that encodes the fabrication sequence, the direction of material deposition can be derived accordingly. In this subsection, we present the computation of local material deposition directions, followed by the constitutive model of anisotropic material in space-time topology optimization.

The direction of material deposition correlates with the gradient of the time field, as depicted in the bottom row of Fig. 1. Shown in Fig. 1(e) is the time field, visualized by a colormap, along with the

isolines, which segment this component into curved layers. In Fig. 1(f), the gradient of the time field is visualized, while Fig. 1(g) additionally displays the tangent of the time field, which defines the material deposition direction. Although the tangent direction is a vector, we do not differentiate whether the material is deposited along the positive or negative direction of the vector, as this has little influence on material anisotropy. We represent the local material deposition direction using the angle formed between the tangent of the time field and the horizontal axis. As shown in Fig. 1(g), the x - y axes are the global reference axes pointing in horizontal and vertical directions. The local material axes x' - y' are aligned with the local material deposition direction, represented by angle θ , which is confined within the range of -90° to 90° .

The local material deposition direction is orthogonal to the gradient of the time field (∇t),

$$\nabla t|_e \cdot \bar{\theta}_e = 0, \quad (4)$$

where $\nabla t|_e$ is the gradient vector of the time field on element e , and $\bar{\theta}_e = [\cos \theta_e, \sin \theta_e]^\top$ is the vector form of the local material deposition direction θ_e . On a structured mesh, the gradient of the time field is calculated using the shape function,

$$\nabla t|_e = \left[\sum_{i \in e} \frac{\partial N_i}{\partial x} t_i, \sum_{i \in e} \frac{\partial N_i}{\partial y} t_i \right]^\top, \quad (5)$$

where $\frac{\partial N_i}{\partial x}$ and $\frac{\partial N_i}{\partial y}$ are the spatial derivative of the shape functions evaluated at the centroid of element e . i is a node of element e , and t_i is the nodal time value. The local material deposition direction, restricted to the range of $[-90^\circ, 90^\circ]$, is calculated by

$$\theta_e = \arctan \left(- \frac{\sum_{i \in e} \frac{\partial N_i}{\partial x} t_i}{\sum_{i \in e} \frac{\partial N_i}{\partial y} t_i} \right). \quad (6)$$

The generalized Hooke's law of an orthotropic material can be found in Appendix A. After obtaining the local material deposition direction θ , the elasticity tensor \mathbf{D} in the global reference axes (x - y) is related to \mathbf{D}_0 in the local material axes (x' - y') by a transformation [51]:

$$\mathbf{D}(\theta) = \mathbf{R}^\top(\theta) \mathbf{D}_0 \mathbf{R}(\theta), \quad (7)$$

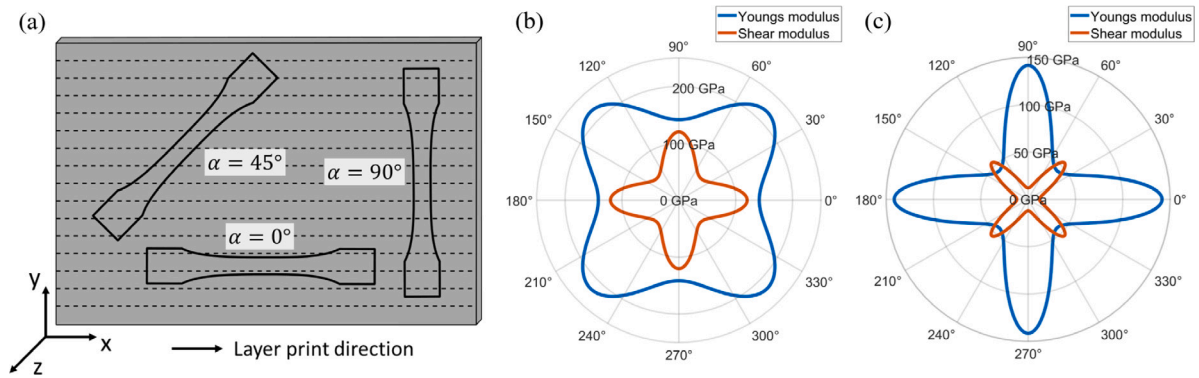


Fig. 2. Anisotropic elasticity in WAAM-processed material. (a) Test samples with different orientations relative to layer print direction. (b) Polar plot of Young's modulus and shear modulus measured in the horizontal axis when the WAAM-processed stainless steel is deposited at different angles (θ). The highest Young's modulus is achieved when the material is deposited at $\pm 45^\circ$. (c) Polar plot of another cubic orthotropic material, whose highest Young's modulus is achieved along or perpendicular to the material deposition direction.

the transformation matrix is

$$\mathbf{R}(\theta) = \begin{bmatrix} \cos^2 \theta & \sin^2 \theta & \sin \theta \cos \theta \\ \sin^2 \theta & \cos^2 \theta & -\sin \theta \cos \theta \\ -2 \sin \theta \cos \theta & 2 \sin \theta \cos \theta & \cos^2 \theta - \sin^2 \theta \end{bmatrix}. \quad (8)$$

Eq. (7) describes the elasticity tensor for a solid element ($\rho_e = 1$) with anisotropic material. For elements with an intermediate density ($\rho_e \in [0.0, 1.0]$), we apply the SIMP interpolation scheme to anisotropic material,

$$\mathbf{D}_e(\rho_e, \theta_e) = \mathbf{R}^T(\theta_e) \mathbf{D}_0(\rho_e) \mathbf{R}(\theta_e) = [\epsilon + (1 - \epsilon)\rho_e^p] \mathbf{R}^T(\theta_e) \mathbf{D}_0 \mathbf{R}(\theta_e), \quad (9)$$

where ϵ is a very small stiffness assigned to void elements to prevent the stiffness matrix from becoming singular. p is a penalization of intermediate densities to promote a black-and-white design (typically $p = 3$).

2.2.1. Material anisotropy in WAAM

Materials processed by metal additive manufacturing exhibit distinctive anisotropic behavior. Here we focus on stainless steel, one of the most common materials used in WAAM. Fig. 2(a) illustrates a thin-walled structure manufactured layer-by-layer using WAAM. The material behavior is measured on samples taken in three directions: along the horizontal layer ($\alpha = 0^\circ$), perpendicular to the layer ($\alpha = 90^\circ$), and with an angle of 45° . According to the experimental data reported by Kyvelou et al. [49], the Young's modulus (slope of the curves) of these samples is different, revealing the anisotropic elasticity. Specifically, the Young's modulus along the layer ($\alpha = 0^\circ$) is very close to that perpendicular to the layer ($\alpha = 90^\circ$); 143.3 GPa and 139.6 GPa, respectively. In contrast, with a Young's modulus of 219.5 GPa, the samples along the 45° direction are significantly stiffer. We note that this anisotropic material behavior differs from the anisotropy in material extrusion 3D printing or fiber-reinforced 3D printing [76], where the material is often stiffest in the deposition direction.

Fig. 2(b) and (c) visualize the modulus in reference axes for finite element analysis, when the material is deposited at different angles (θ). The plots in Fig. 2(b) correspond to the WAAM-produced stainless steel. Considering the nearly identical values of the Young's modulus along and perpendicular to the layer (143.3 GPa and 139.6 GPa, respectively), we simplify by setting E_x and E_y to the same value, $E_x = E_y = 141.45$ GPa, indicating a cubic orthotropic material. The Poisson's ratio in this context is $\nu_{xy} = \nu_{yx} = 0.30$. The shear modulus of this material reaches its peak when the material is deposited along the horizontal reference axis ($\theta = 0^\circ$). The stiffest direction of this material appears at $\theta = \pm 45^\circ$ with $E_{\pm 45^\circ} = 219.50$ GPa, conforming to Fig. 2(b).

As a comparison, Fig. 2(c) plots the Young's modulus and shear modulus of a different material for various material deposition directions. At $\theta = 0^\circ$, this material shares the same Young's modulus

($E = 141.45$ GPa) as with the material in Fig. 2(b). However, its shear modulus is minimal at $\theta = 0^\circ$. This material is stiffer along (and perpendicular to) the deposition direction $\theta = 0^\circ$ than along other directions. While such behavior differs from that observed in WAAM-processed metals, we employ it in our results section for a comparative study investigating the influence of material properties on fabrication sequence optimization.

2.3. Computational workflow

This section presents key steps in the computational workflow of space-time topology optimization, including the regularization of the time field (Section 2.3.1) and the filtering and projection procedures (Section 2.3.2).

Fig. 3 depicts the computational workflow of space-time topology optimization, with the integration of the anisotropic material model. We employ the space-time optimization framework recently proposed by Wang et al. [77]. Rather than directly taking the time field as optimization variables, this framework introduces auxiliary variables μ and a partial differential equation to implicitly define the time field, avoiding local minima that may appear when the time field is directly optimized. Specifically, as will be elaborated in Section 2.3.1, the time field t is computed by solving a heat equation, based on the density field ρ that represents the structural layout, and a thermal diffusivity field $\bar{\mu}$. The density and thermal diffusivity fields are filtered versions of optimization variables φ and μ , respectively. The filtering procedure is common in density-based topology optimization, and thus omitted in the illustration but will be explained in Section 2.3.2. From the time field, the material deposition direction is calculated, accordingly to Section 2.2. By combining the density and time fields, intermediate structures are computed, as introduced in Section 2.1. Afterward, the stiffness matrix of intermediate structures is calculated, taking the material anisotropy into account (Section 2.2.1). This is then used to analyze the response of intermediate structures. Based on the response functions, as well as the sensitivities, the optimization variables are updated.

2.3.1. Regularization of the time field

As discussed in Section 2.1, we use a time field to encode the fabrication sequence, with a larger time value indicating that the corresponding location is intended for fabrication at a later stage. Isolines of this scalar field divide the structural layout into curved layers. This parameterization of the fabrication process opens up a huge solution space. However, the sequence represented by the isolines does not guarantee manufacturability. Ensuring fabrication continuity is crucial among the manufacturability constraints: material should

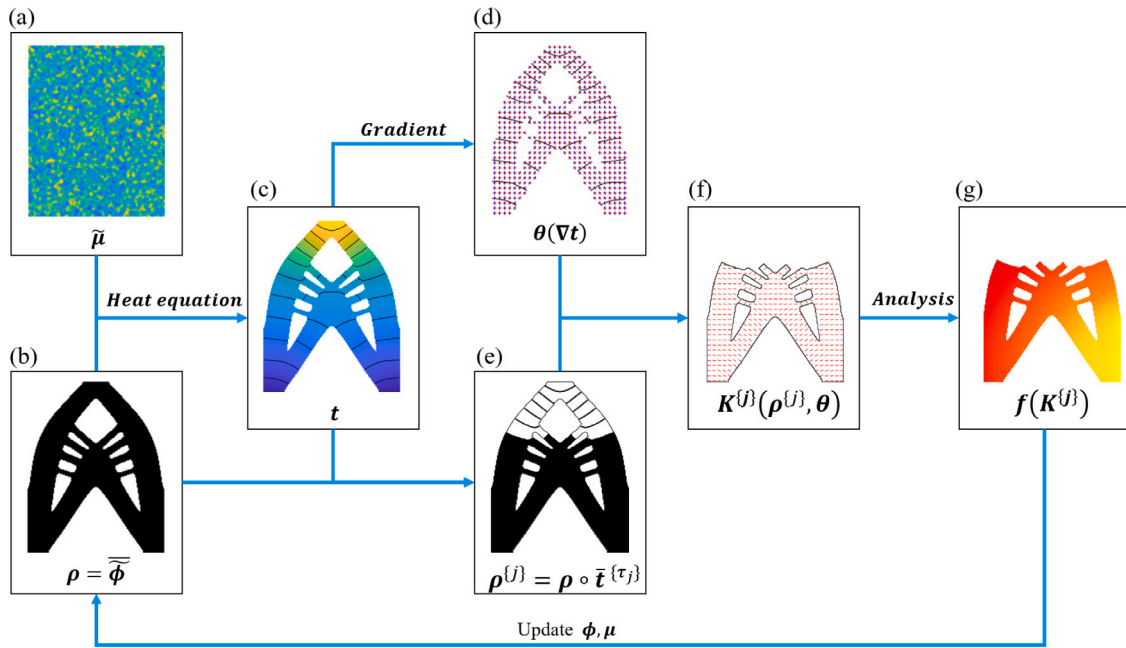


Fig. 3. Workflow of space-time topology optimization considering material anisotropy. (a) The heat diffusivity field. (b) The physical density field. (c) The pseudo-time field obtained from solving the heat equation Eq. (11). (d) Material orientation field obtained through the orthogonal relationship as in Eq. (4). (e) The j th intermediate structure represented as in Eq. (2). (f) The mechanical properties of the intermediate structure. (g) The mechanical analysis of the intermediate structure.

only be deposited on already produced parts or directly onto the build plate. This requires the time field to be free of local minima.

To address this issue, Wang et al. proposed to regularize the time field using a heat equation. Assuming a virtual heat source (with a constant temperature of 1) at the build plate, this creates a virtual temperature field that gradually decreases. The temperature field (T) is continuous and free of local maxima. Its inverse is interpreted as the time field,

$$t = 1 - T. \quad (10)$$

We note that the virtual heat source is introduced to create a continuous scalar field, and shall not be confused with the thermomechanical process during additive manufacturing.

The virtual temperature field is determined by locally varying thermal diffusivity (μ) across the domain, treated as optimization variables to steer the fabrication sequence. It is further coupled with the density field to reflect the influence of the structural layout. The heat equation takes the form of

$$\nabla(\rho\tilde{\mu}\nabla T) - \alpha_T T = 0. \quad (11)$$

Here ∇ is the vector differential operator. ρ is the density, obtained from the design variable $\phi \in [0.0, 1.0]$. $\tilde{\mu}$ represents the pseudo thermal diffusivity. It is obtained from a new set of optimization variables $\mu \in [0.0, 1.0]$. α_T denotes a constant drain rate.

Using the finite element method, the heat equation is discretized into a linear form,

$$\mathbf{K}_T(\rho, \tilde{\mu})\mathbf{T} = \mathbf{b}, \quad (12)$$

where \mathbf{K}_T is the thermal stiffness matrix. \mathbf{T} denotes the nodal temperature vector. \mathbf{b} represents the thermal load vector specifying the virtual heat source, corresponding to the region where manufacturing is prescribed to start. Bi-linear interpolation is used to obtain the temperature field on the elements.

The thermal stiffness matrix consists of two parts,

$$\begin{aligned} \mathbf{K}_T^e(\rho, \tilde{\mu}) &= \int_{\Omega_e} \rho_e \tilde{\mu}_e \left(\frac{\partial N_i}{\partial x} \frac{\partial N_j}{\partial x} + \frac{\partial N_i}{\partial y} \frac{\partial N_j}{\partial y} \right) d\Omega_e \\ &+ \int_{\Omega_e} \alpha_T N_i N_j d\Omega_e. \end{aligned} \quad (13)$$

The first part corresponds to the thermal diffusivity, while the second part represents the drain term. N_i and N_j are the shape functions.

2.3.2. Filtering and projection procedures

Filtering of the design variables is important in density-based topology optimization to avoid checkerboard problems for low-order elements [78]. We use the convolution filter as introduced in [79,80] for the density field:

$$\tilde{\phi}_e = \frac{\sum_{i \in \mathbb{N}_e} H(\mathbf{x}_i) \phi_i}{\sum_{i \in \mathbb{N}_e} H(\mathbf{x}_i)}, \quad (14)$$

where \mathbb{N}_e is the neighborhood set of element e , including elements whose distance to element e is less than a given radius R_e . \mathbf{x}_i denotes the centroid of element i . The weighting factor of an element linearly decreases according to its distance to \mathbf{x}_e ,

$$H(\mathbf{x}_i) = R_e - \|\mathbf{x}_i - \mathbf{x}_e\|. \quad (15)$$

The filtering is followed by a projection to promote a black-and-white design. We use the tanh function [81,82]:

$$\rho_e = \tilde{\phi}_e = \frac{\tanh(\beta_d \eta) + \tanh(\beta_d (\tilde{\phi}_e - \eta))}{\tanh(\beta_d \eta) + \tanh(\beta_d (1 - \eta))}. \quad (16)$$

This function projects values larger than η to one, and those less than η to zero. η is set to 0.5. The parameter β_d controls the sharpness of projection. A continuous is applied in optimization; the optimization starts with a small β_d and gradually increases it after a fixed number of iterations. The obtained physical density ρ is used in the structural analysis and the heat equation Eq. (11).

Filtering is also necessary for the second set of optimization variables, μ . We use the same filtering technique as for the density field, but note that the filter radius and weighting functions for ρ and μ are not necessarily the same:

$$\tilde{\mu}_e = \frac{\sum_{i \in \mathbb{N}_e} H(\mathbf{x}_i) \mu_i}{\sum_{i \in \mathbb{N}_e} H(\mathbf{x}_i)}. \quad (17)$$

The filtering of the thermal diffusivity field is important to increase the smoothness of the time field, which contributes to the smoothness of the local material orientation.

2.3.3. Space–time topology optimization for anisotropic material

In space–time topology optimization, the objective includes performance measures of both intermediate structures during fabrication and the final structure. It should be noted that the intermediate structures and the final structure can have different boundary conditions and load cases. The boundary conditions of the intermediate structures correspond to the manufacturing process, whereas the boundary conditions for the final structure relate to its intended use scenario. The optimization problem is formulated as follows:

$$\min_{\phi, \mu} f_0 = c_0 + \sum_{j=1}^N w_j c_j, \quad (18)$$

$$\text{s.t.} \quad \mathbf{K}(\rho, \theta) \mathbf{U} = \mathbf{F}, \quad (19)$$

$$\mathbf{K}^{(j)}(\rho^{(j)}, \theta) \mathbf{U}^{(j)} = \mathbf{G}^{(j)}, \quad j = 1, 2, \dots, N, \quad (20)$$

$$g_0 = \sum \rho_e v_e \leq V_0, \quad (21)$$

$$g_j = \sum \rho_e^{(j)} v_e \leq \frac{j}{N} V_0, \quad j = 1, 2, \dots, N, \quad (22)$$

$$0.0 \leq \phi_e \leq 1.0, \quad (23)$$

$$0.0 \leq \mu_e \leq 1.0, \quad (24)$$

where N is the prescribed number of layers or intermediate structures. $c_0 = \mathbf{U}^\top \mathbf{K} \mathbf{U}$ is the compliance of the final structure, and $c_j = (\mathbf{U}^{(j)})^\top \mathbf{K}^{(j)} \mathbf{U}^{(j)}$ is the compliance of the j th intermediate structure. The compliances are weighted by w_j .

Eqs. (19) and (20) describe the governing equations of the final structure and intermediate structures, respectively. \mathbf{F} is the external load for the final structure. $\mathbf{G}^{(j)}$ is the load applied on the j th intermediate structure, such as the structure's self-weight, the weight of the robotic arm, or thermal-induced loads. The stiffness matrices of intermediate structures are a function of $\rho^{(j)}$ and θ . $\rho^{(j)}$ is the material distribution of the j th intermediate structure, corresponding to the time point τ_j . It is obtained by re-writing Eq. (2) in a vector form, $\rho^{(j)} = \rho \circ \mathbf{t}^{\tau_j}$, with \circ denoting the Hadamard product of two vectors. θ is derived from the time field (Eq. (6)).

Eqs. (21) and (22) prescribe the volume of the entire structure and intermediate structures, respectively. V_0 is the total material budget, and v_e is the volume of each element. Assuming a constant material deposition rate, the volume increase per layer is constant, i.e., $\frac{1}{N} V_0$.

The optimization includes two sets of variables, each ranging between 0.0 and 1.0. By fixing the density field and excluding it from the design update, the formulation is simplified to optimize only the fabrication sequence.

We solve the optimization problem by using the method of moving asymptotes (MMA) [83]. The sensitivity analysis is detailed in the Appendix B. Algorithm 1 details the optimization process. The optimization stopping criteria is either the design change Δ is smaller than a certain value, e.g., $\epsilon_{\text{lim}} = 1e-5$ or the number of total iterations reaches the maximum iteration step It_{max} .

3. Numerical examples

In this section, we validate the proposed method through multiple numerical examples. We start by comparing the fabrication sequences optimized with different types of material anisotropy, using a simple geometry (Section 3.1), followed by fabrication sequence optimization of a mechanical component (Section 3.2). We then proceed to validate the effects of material anisotropy in space–time topology optimization, considering the self-weight of intermediate structures (Section 3.3) and the weight of a mobile robotic platform on intermediate structures (Section 3.4). All examples are in 2D and under the plane stress condition. Each optimization involves 600 iterations.

Algorithm 1 Space–time topology optimization for anisotropic materials

Input: Total material volume V_0 and number of layers N

Output: Optimized density field ρ and time field t

```

1: Design variables initialization  $\phi = \phi_0, \mu = \mu_0$ 
2: Iteration index  $itr = 0$ 
3: Design change  $\Delta = 1.0$ 
4: Projection parameters  $\beta_i = 10.0, \beta_d = 1.0$ 
5: while  $\Delta \geq \epsilon_{\text{lim}}$  and  $itr \leq \text{It}_{\text{max}}$  do
6:    $itr = itr + 1$ 
7:    $\rho = \bar{\phi} \leftarrow \bar{\phi} \leftarrow \phi$  via Eq. (14) and Eq. (16)
8:    $\bar{\mu} \leftarrow \mu$  via Eq. (17)
9:    $\mathbf{K}_T \leftarrow \rho, \bar{\mu}$  via Eq. (13)
10:   $t = 1 - T$  via solving Eq. (12)
11:   $\nabla t \leftarrow t$  via Eq. (5)
12:   $\theta \leftarrow \nabla t$  via Eq. (4)
13:   $\mathbf{K} \leftarrow \rho, \theta$  via Eq. (9)
14:   $\mathbf{U} \leftarrow \mathbf{K}$  via solving Eq. (19)
15:   $c_0 \leftarrow \mathbf{K}, \mathbf{U}$ 
16:   $\frac{\partial c_0}{\partial \phi}, \frac{\partial c_0}{\partial \mu}$  as formulated in Appendix.
17:  for  $j = 1$  to  $N$  do
18:     $\rho^{(j)} \leftarrow \rho, t$  via Eq. (2)
19:     $\mathbf{K}^{(j)} \leftarrow \rho^{(j)}, \theta$  via Eq. (9)
20:     $\mathbf{U}^{(j)} \leftarrow \mathbf{K}^{(j)}$  via solving Eq. (20)
21:     $c_j \leftarrow \mathbf{K}^{(j)}, \mathbf{U}^{(j)}$ 
22:     $\frac{\partial c_j}{\partial \phi}, \frac{\partial c_j}{\partial \mu}$  as formulated in Appendix.
23:  end for
24:   $\phi, \mu \leftarrow \frac{\partial c_0}{\partial \phi}, \frac{\partial c_0}{\partial \mu}, \frac{\partial c_j}{\partial \phi}, \frac{\partial c_j}{\partial \mu}$  via MMA solver
25:   $\Delta = \max_{ve} (|\phi_e^{itr} - \phi_e^{itr-1}|, |\mu_e^{itr} - \mu_e^{itr-1}|)$ 
26:  if  $\text{mod}(itr, 50) = 0$  then
27:     $\beta_i = \beta_i + 10.0$ 
28:     $\beta_d = \beta_d \times 2$ 
29:  end if
30: end while

```

3.1. Anisotropic materials

To investigate the effects of material anisotropy on design optimization, we consider two simple load cases where a rectangular shape is under pure tension or shear stress, as illustrated in Fig. 4(a) and Fig. 5(a), respectively. We optimize the fabrication sequence to produce this rectangular shape, i.e., the density field is kept constant and excluded from optimization, while the time field is to be optimized. The objective is to minimize the compliance of the shape as it is fully fabricated. No performance characteristics of intermediate structures are included in the objective. The compliance of the entire shape depends on the orientation of the anisotropic material, which is governed by the fabrication sequence. The fabrication is prescribed to start from the bottom of the domain, and finish with 10 layers. The domain is discretized into a regular grid of 40 by 40 finite elements.

We test sequence optimization with two anisotropic materials, as previously introduced in Section 2.2.1 and illustrated in Fig. 2. The material properties are summarized in Table 1. Material-1 has a high shear modulus. Its stiffest direction is at 45° to the layer orientation, i.e., $\theta = \pm 45^\circ$. In contrast, the shear modulus of Material-2 is low. Its stiffest direction is along and perpendicular to the layer, i.e., $\theta = 0^\circ$ and $\theta = 90^\circ$.

In the uniaxial tension case (Fig. 4), the major principal stress is horizontal, shown in (e). The fabrication sequences, optimized with Material-1 and Material-2, are shown in the first row (b, c, d) and second row (f, g, h), respectively. With the high-shear material, the layers are oriented at $\pm 45^\circ$ to the x -axis (b, c). In contrast, with the low-shear material, the layers are horizontal (f, g). However, with both

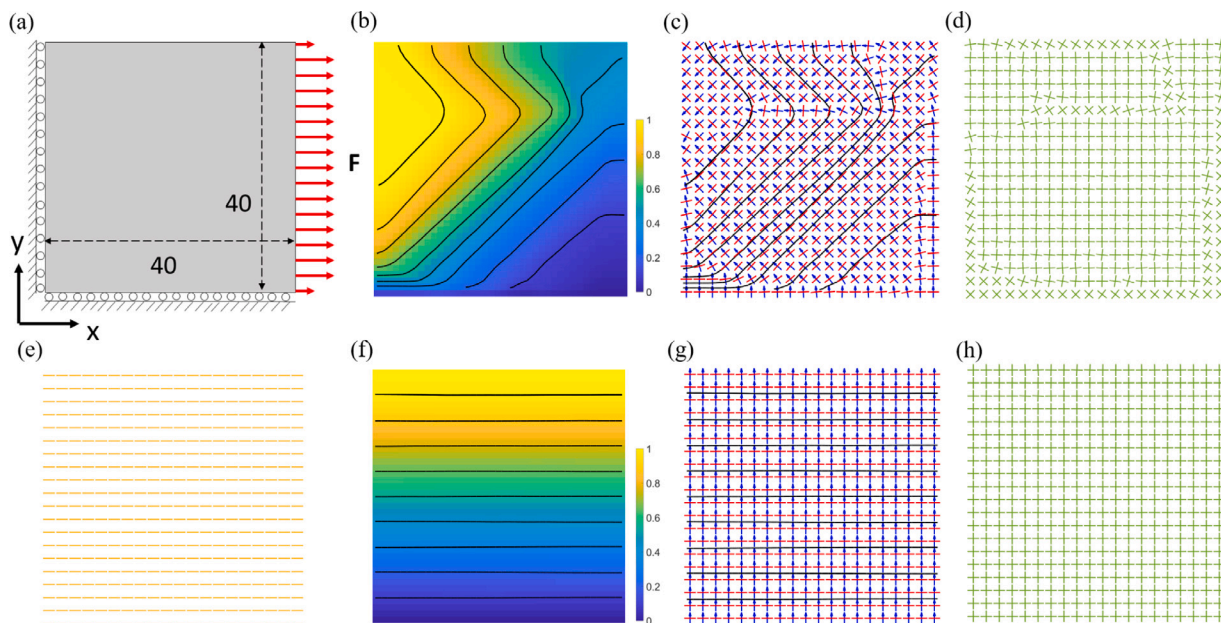


Fig. 4. Comparison of optimized fabrication sequences for anisotropic materials with high-shear and low-shear modulus, tested for uniaxial tension condition. (a) A rectangular component under uniaxial tension. (e) The optimal orientation of the stiffest direction of the material (major principal stress direction) is horizontal. For anisotropic materials with high-shear modulus: (b) The optimized time field with isolines, representing the optimized fabrication sequence, (c) The gradient direction of the time field (blue arrows) and the corresponding material orientation (red lines), (d) The two orthogonal stiffest directions of the anisotropic material. In the same order, (f–h) depict the results for anisotropic materials with low-shear modulus.

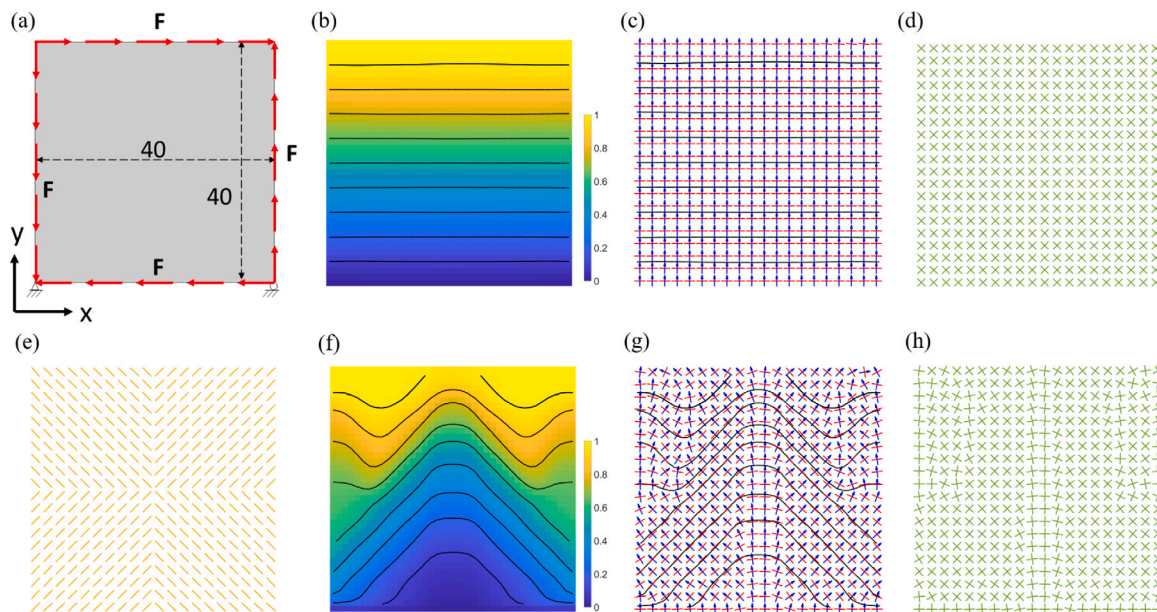


Fig. 5. Comparison of optimized fabrication sequences for anisotropic materials with high-shear and low-shear modulus, tested for pure shear stress condition. (a) A rectangular component under pure shear stress. (e) The optimal orientation of the stiffest direction of the material (major principal stress direction) is at $\pm 45^\circ$ to the x -axis. For anisotropic materials with high-shear modulus: (b) The optimized time field with isolines, representing the optimized fabrication sequence, (c) The gradient direction of the time field (blue arrows) and the corresponding material orientation (red lines), (d) The two orthogonal stiffest directions of the anisotropic material. In the same order, (f–h) depict the results for anisotropic materials with low-shear modulus.

Table 1
Material properties of two anisotropic materials. The unit of elastic modulus is GPa.

	E_x	E_y	G_{xy}	ν_{xy}
Material-1	141.45	141.45	120.10	0.3
Material-2	141.45	141.45	12.01	0.3

materials, the stiffest material direction is primarily along the x - and y -axis (d, h), in agreement with the major principal stress direction (e).

An alignment of the stiffest material direction to the major principal stress is also observed in the case of pure shear stress (Fig. 5). In the first row, corresponding to the high-shear material, the optimized layers are horizontal (b, c), resulting in the stiffest material direction at $\pm 45^\circ$ to the x -axis (d). In the second row, with the low-shear material, the optimized layers are curved, and mostly at $\pm 45^\circ$ to the x -axis (f, g), leading to the stiffest material direction at $\pm 45^\circ$ to the x -axis (h).

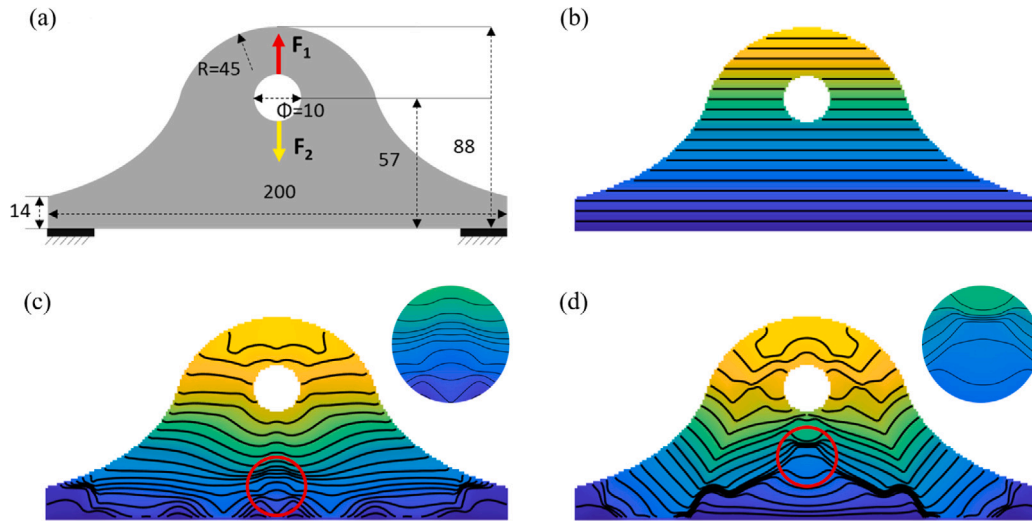


Fig. 6. Fabrication sequence optimization for an engineering component. (a) The bracket and boundary conditions for its intended use scenario. (b) Planar fabrication process as a reference. (c, d) Optimized time field and isolines, representing the optimized fabrication sequence, obtained using the anisotropic material with (c) high-shear modulus, Material-1 and (d) with low-shear modulus, Material-2.

3.2. Fabrication sequence optimization

The third example of fabrication sequence optimization is a bracket shown in Fig. 6. The bracket is clamped at its bottom, on the left and right. It has two alternating loads on its inner circle, pointing upwards and downwards. The objective is to minimize the compliance of the component subject to both loading conditions. Similar to previous examples, the fabrication is prescribed to start from the bottom. The prescribed number of layers is 20.

The optimized fabrication sequence using Material-1 is shown in Fig. 6(c). It is symmetric due to the symmetric boundary conditions and structural layout. For comparison, the planar fabrication sequence is illustrated in Fig. 6(b). The component manufactured using planar layers has the compliances of $c_1 = 98.85$ and $c_2 = 92.59$ for the two loads, while according to the optimized fabrication sequence in Fig. 6(b) it has the compliances of $c_1 = 91.75$ and $c_2 = 88.61$. The smaller compliances confirm that by optimizing the fabrication sequence, the mechanical capabilities of the final structure can be enhanced through the effective utilization of material anisotropy.

We note that the improvement in structural performance through fabrication sequence optimization depends on the extent of material anisotropy. When repeating the fabrication sequence optimization with Material-2, the improvement in structural performance compared to planar layers is more significant. The optimized sequence is illustrated in Fig. 6(d). In most areas, the layer orientation differs from that of Material-1 by $\pm 45^\circ$. The component manufactured using planar layers with Material-2 has compliances of $c_1 = 321.0$ and $c_2 = 336.1$ for the two loads. In contrast, the component produced with the optimized fabrication sequence shown in Fig. 6(d) has compliances of $c_1 = 163.6$ and $c_2 = 154.2$. This optimization reduces the sum of compliances by 51.64%.

Material-2 has its stiffest direction aligned with the material deposition direction. For single-load cases, arranging the material along the principal stress distribution results in a stiff structure. For two load cases, aligning the material direction according to the principal stress of one load case improves the stiffness for that specific load but leaves the performance under the other load unoptimized. In this example, aligning the material deposition direction with the principal stress direction of the first load case, F_1 , results in structural compliances of $c_1 = 142.9$ and $c_2 = 195.3$. Conversely, using the principal stress directions of the second load case, F_2 , yields compliances of $c_1 = 197.9$ and $c_2 = 137.6$. The sums of these compliances are 6.42% and 5.57%

higher, respectively, than those achieved with the optimized sequence considering both loads simultaneously.

The examples above have demonstrated that the optimized fabrication sequence is influenced by the anisotropic characteristics of the material. In the following section, we will continue with the high-shear material model (Material-1), which corresponds to WAAM-processed austenitic stainless steel.

3.3. Space-time optimization for self-weight

After demonstrating the impact of fabrication sequence on material anisotropy and, consequently, on structural performance, we proceed to showcase the importance of incorporating material anisotropy in space-time topology optimization. The structural layout and fabrication sequence will collectively exploit the anisotropic characteristics of material stiffness.

This example concerns a vertically oriented beam, as shown in Fig. 7(a). The rectangular design domain is discretized into 100×400 finite elements. The objective is to minimize the compliance of the entire structure in its intended use scenario (c_0) and the compliance of intermediate structures during fabrication ($\sum c_j$). In the use scenario, *i.e.*, after the beam has been fully fabricated, it is fixed at its bottom and supports a horizontal load at its top. The fabrication process starts from the bottom, assuming the bottom of the beam is fixed on a horizontal baseplate. Throughout fabrication, the intermediate structure supports the gravitational load of its own weight. This load is dependent on both the structural layout and fabrication sequence. The total weight of the structure equals the magnitude of the external force F applied during its use scenario.

Some key parameters for optimization are outlined below: The entire structure is segmented into $N = 20$ or 40 layers for manufacturing. The weight coefficients assigned to compliances of intermediate structures in the objective function are set to $w_j = 1/N$. The volume fraction of the entire structure is fixed at 0.5. The filter radius for the density and heat conductivity fields is set to 3 times the length of a single element. The material property corresponding to the WAAM-produced stainless steel (Material-1) is utilized.

The optimized results with $N = 20$ are visualized in Fig. 7(b–d). Fig. 7(b) shows the optimized structural layout, represented by the physical density field after filtering and projection. In Fig. 7(c), the structural layout is color-coded according to the time field, illustrating the fabrication sequence. The isolines of the time field, indicated by the black lines, outline the boundaries of layers. The layers are sequentially

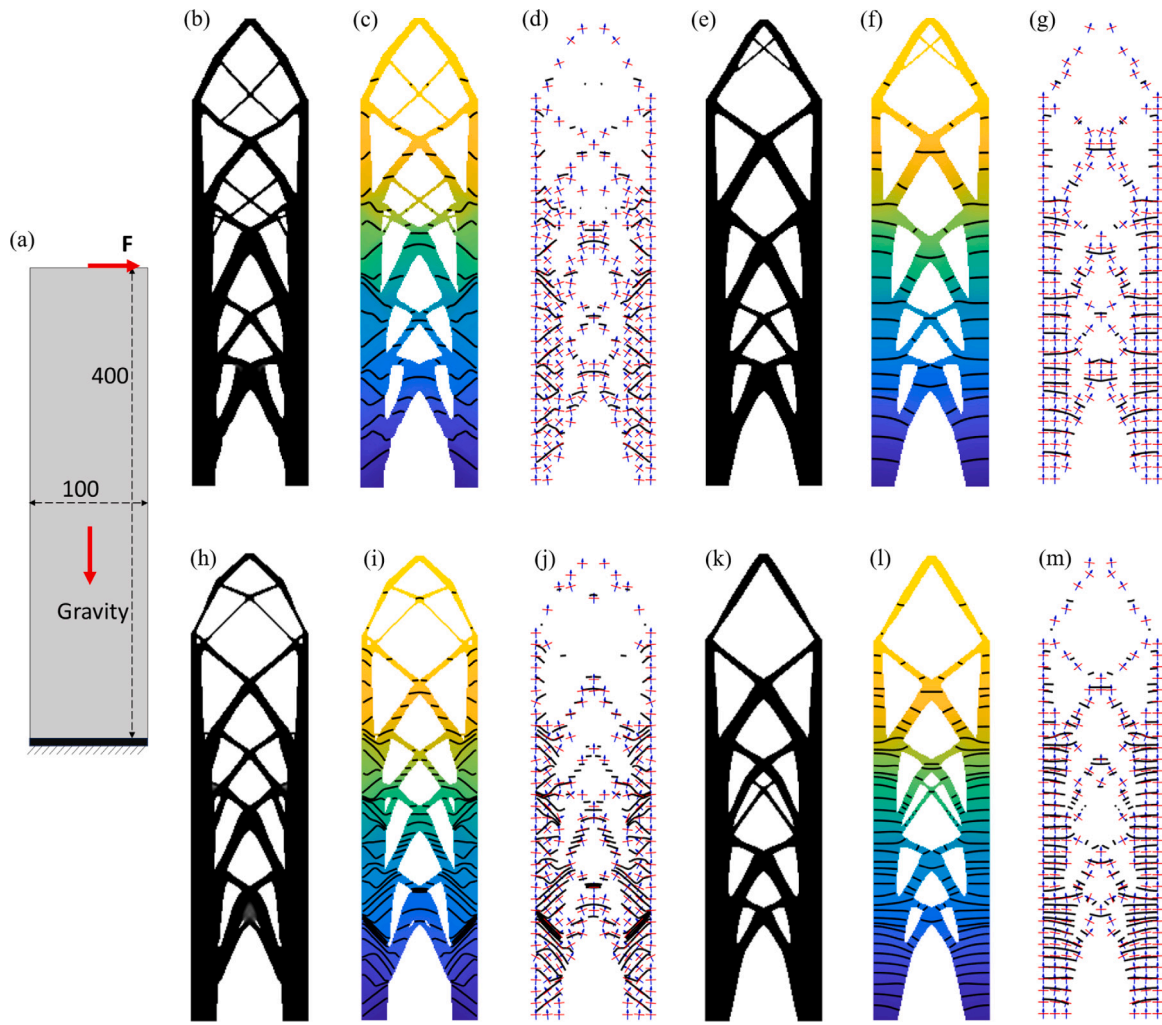


Fig. 7. Space-time topology optimization of a vertical beam. (a) Design domain of a vertical beam, consider the self-weight of the structure during fabrication, and an external load (F) on the fully fabricated structure. The optimization is performed in four different setups. Top row (b–g): $N = 20$, with anisotropic material (b, c, d) and isotropic material (e, f, g). Bottom row (h–m): $N = 40$, with anisotropic material (h, i, j) and isotropic material (k, l, m). For each setup, from left to right: Optimized structural layout, optimized structure color-coded by the optimized time field, and gradient directions and the corresponding material orientations.

Table 2

Mechanical performances of a vertically oriented beam, considering the self-weight of intermediate structures.

	Compliances (scaled)	Optimization result			Analysis with anisotropic material		
		c_0	$\sum c_j$	$f_0 = c_0 + \sum w_j c_j$	c_0	$\sum c_j$	$c_0 + \sum w_j c_j$
$N = 20$	Optimized with anisotropic material	98.76	1.00	98.81	98.76	1.00	98.81
	Optimized with isotropic material	138.55	1.21	138.62	134.19	1.19	134.25
$N = 40$	Optimized with anisotropic material	99.82	1.68	99.86	99.82	1.68	99.86
	Optimized with isotropic material	140.52	2.14	140.57	134.48	2.09	134.54

stacked from the bottom. In Fig. 7(d), the gradient direction of the optimized time field and the material orientation are depicted, which are orthogonal. The material orientations are observed to generally align with the layer boundaries, as in all examples.

The compliance of the final structure under the external force is $c_0 = 1825.85$, and the sum of compliances of intermediate structures under their own weight is $\sum c_j = 18.49$. For an easy comparison to variations later on, we scale these values by dividing $\sum c_j$, leading to $c_0 = 98.76$ and $\sum c_j = 1.00$. The same scaling factor is applied to other designs in this section. As a comparison, if the optimized structure is to be manufactured using planar layers, the compliances become $c_0 = 131.62$ and $\sum c_j = 1.31$. Both are larger in comparison to the design with optimized curved layers and material orientations. This confirms the advantage of optimizing the fabrication sequences along with the structural design using space-time topology optimization.

In a further comparative study, we optimize the beam using an isotropic material to reveal the differences in structural layout and fabrication sequence with and without material anisotropy. The property of the isotropic material is: $E_x = 141.45$ GPa, $E_y = 141.45$ GPa, $\nu_{xy} = 0.30$, $G_{xy} = E_x/2(1 + \nu) = 54.40$ GPa. As the material is isotropic, the material orientation does not influence structural performance. The optimized results are shown in Fig. 7(e–g). The optimized structural layout displayed in Fig. 7(e) is rather similar to that in Fig. 7(b), while the optimized fabrication sequences differ more. The whole structure's compliance is $c_0 = 138.55$, and the sum of intermediate structures' compliances is $\sum c_j = 1.21$. For a fair comparison, we conduct a post-analysis on the optimized structural layout and fabrication sequence, using the anisotropic material in replacement of the isotropic one. The results are summarized in Table 2. The compliances resulting from the optimization using the anisotropic material are 26.54% smaller

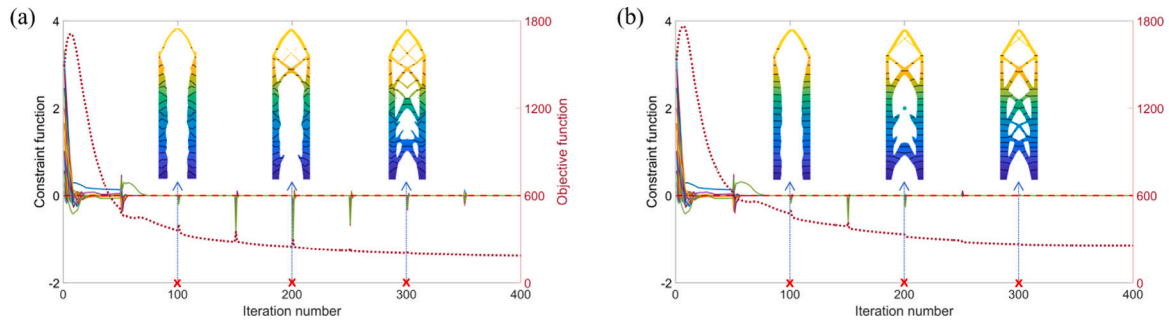


Fig. 8. Convergence curves of the objective function and constraints for anisotropic (a) and isotropic material (b). The two plots correspond to the final designs shown in Fig. 7(c) and (f), respectively.

than those using the isotropic material. Both the compliance of the final structure and that of intermediate structures are improved when material anisotropy is included in space–time topology optimization.

The same conclusion holds when the structure and sequence are optimized with 40 layers. The optimized results using anisotropic and isotropic materials are shown in the second row in Fig. 7, and their corresponding structural performances are included in Table 2. Compared to the compliances with $N = 20$, the optimization with more layers results in slightly increased compliances. This is because the constraints are more strict as the granularity of the fabrication sequence increases.

In addition, Fig. 8 shows convergence curves of the objective function and constraint functions corresponding to the results in Fig. 7(c) and (f). In both scenarios, the objective function (red dotted line) stably decreases, and all the constraint functions converge to zero. The slight discontinuities in the curves, which occur every 50 iterations, are due to the continuation scheme of the projection parameters β_i and β_d . The designs at the 100-th, 200-th, and 300-th iteration are included in the figures. Both scenarios show comparable convergence, with the isotropic scenario converging somewhat faster, suggesting added complexity introduced by the anisotropic material. The objective function with the anisotropic material converges to a smaller value than with the isotropic material.

3.4. Space–time optimization for a mobile robot

Our last example is the construction of a large cantilever beam using a mobile robotic platform, inspired by an artistic illustration from MX3D. The artistic illustration and the simplified model for space–time optimization are shown in Fig. 9(a, b). Similar to the previous example, the objective is to minimize the compliance of the entire structure (c_0) and compliance of intermediate structures ($\sum c_j$). However, for intermediate structures, rather than the self-weight of the structure, we consider the weight of the mobile robot. The full structure is anchored on the left and supports an external load on the right ($F = 5000$ N). The fabrication is prescribed to start from the edge on the left. During fabrication, the intermediate structure provides support to the mobile robotic platform, which moves from left to right. It is assumed that the robot moves at a constant speed and its weight is also constant ($G = 1000$ N). At the i th stage in fabrication, the robot is located at a distance of $\frac{i-1}{N}L_x$ to the left edge, where N is the number of stages and $L_x = 160$ represents the length of the domain. The key optimization parameters remain the same as in the previous example.

The results optimized using both the anisotropic and isotropic material are shown in Fig. 9. As can be seen from (c, f), the optimized structural layouts using the two different materials are quite similar. The overhang feature in the top right of the domain might not seem intuitive. It is created to support the last location of the robotic platform. The fabrication sequences differ for the two materials. For example, for the part of structures dominated by tension (marked by the red box), for the anisotropic material the layers are more curved, while for

the isotropic material, the layers are close to planar. The anisotropic material is oriented in such a way to make use of its stiffer directions.

Fig. 9(i) shows the manufacturing process according to the optimized fabrication sequence in Fig. 9(d). The positions where the mobile robot is located during manufacturing are marked in red bricks on the top boundary. It can be seen that the intermediate structure provides support to the mobile robot.

Comparisons of mechanical performances between the results optimized using anisotropic and isotropic materials are included in Table 3. The compliance values are scaled for clarity. The overall performance, measured as $c_0 + \sum w_j c_j$, of the result optimized using the anisotropic material is smaller, which again confirms the benefit of incorporating manufacturing-induced material anisotropy into space–time topology optimization. This performance gain is primarily due to the improved performance of the entire structure (100.00 vs 125.28).

4. Conclusions and future work

In this paper, we have introduced a space–time topology optimization method that accounts for elastic anisotropy in WAAM-processed material. We utilize a pseudo-density field to represent the structural layout and a pseudo-time field to encode the fabrication sequence. The orientation of anisotropic materials is determined from the pseudo-time field, with the local material deposition direction orthogonal to the gradient of the time field. Our numerical study focuses on anisotropic stiffness, and we anticipate that extending this approach to consider anisotropic strength is feasible since the anisotropic direction has already been derived from the optimization variables.

Our results prove the possibility and benefits of incorporating material anisotropy into structural design and process planning. Firstly, by examples of fabrication sequence optimization, we have shown that leveraging elastic anisotropy can enhance mechanical performance. Unlike planar fabrication sequences in conventional 2.5D printing, optimized fabrication sequences align material deposition orientations to take advantage of the stiffer direction of materials. It was observed that the anisotropic characteristic (high-shear vs low-shear modulus) significantly influences the optimization results. Secondly, incorporating material anisotropy into space–time topology optimization also yields distinct structural layouts and fabrication sequences compared to those based on isotropic materials. Leveraging material anisotropy proves to be an effective approach to enhancing the performance of intermediate structures as well as the overall structure.

Future work. The work presented in this paper provides a strong foundation for exploring the full potential of robot-assisted additive manufacturing. However, further advancements are necessary to achieve experimental validation of the innovative fabrication sequences proposed. One of the primary challenges lies in accurately producing layers with significant thickness variations, even when utilizing multi-axis printing. To address this, it is essential to limit these variations within the computational design method and implement adaptive adjustments

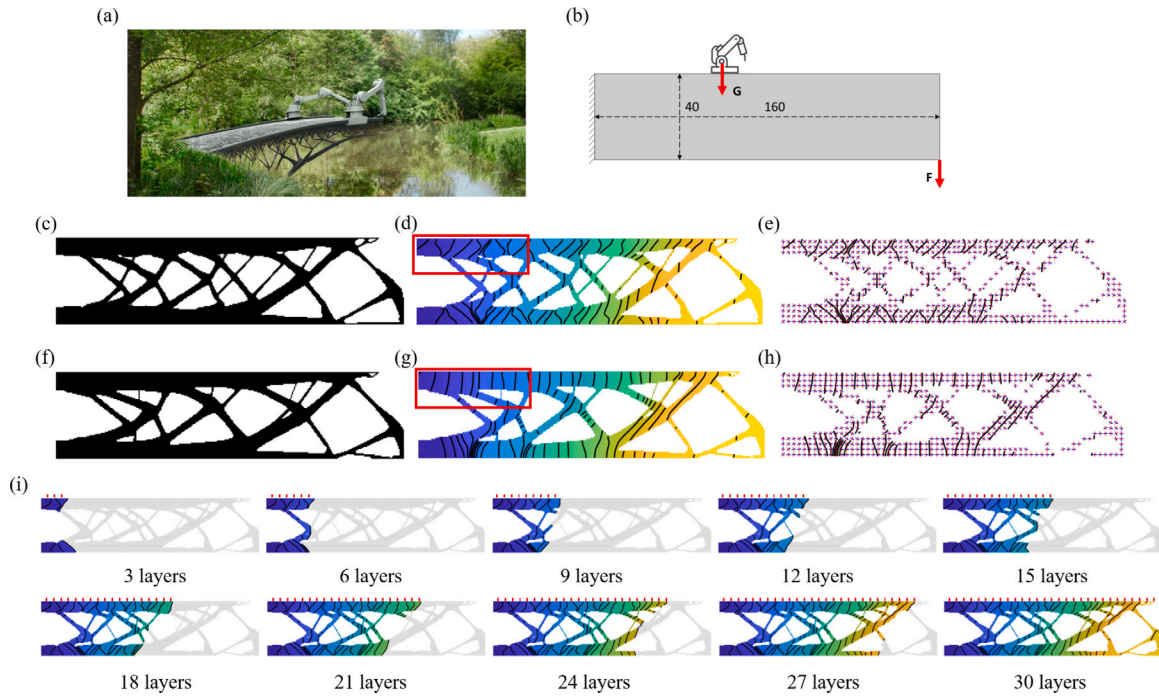


Fig. 9. Space-time topology optimization of a cantilever beam. (a) Artistic illustration of building a bridge with a robot moving on top of it. The bridge under construction shall support the mobile robotic platform at all intermediate stages. Image courtesy of MX3D (www.mx3d.com). (b) Simplified design domain of the cantilever bridge, consider the weight of a robotic platform during fabrication, and an external load (F) on the fully fabricated structure. (c–h) The optimization results for anisotropic material (c–e) and isotropic material (f–h). From left to right: Optimized structural layout (c, f), optimized structure color-coded by the optimized time field (d, g), gradient directions and the corresponding material orientations (e, h). (i) Illustration of the manufacturing process according to the optimized fabrication sequence in (d), the locations of the robotic platform on the top of the domain are marked in red bricks.

Table 3

Mechanical performances of a cantilever beam, considering the weight of a mobile robot on intermediate structures.

	Compliances (scaled)	Optimization result			Analysis with anisotropic material		
		c_0	$\sum c_j$	$f_0 = c_0 + \sum w_j c_j$	c_0	$\sum c_j$	$c_0 + \sum w_j c_j$
$N = 30$	Optimized with anisotropic material	100.00	57.22	101.97	100.00	57.22	101.97
	Optimized with isotropic material	134.58	72.22	137.07	125.28	64.92	127.52

to process parameters during manufacturing, to account for the impact of the curved fabrication on the geometry of layer beads. Additionally, incorporating advanced models of the WAAM (Wire Arc Additive Manufacturing) process, including factors such as metal transfer modes and intermediate cooling processes, would enhance the accuracy of predictions regarding mechanical properties and manufacturing precision. However, this approach demands intensive computational resources, as performance predictions are required at each iteration of the optimization process. Lastly, our current method is primarily for the manufacturing of thin-walled structures. Extending this approach to bulkier 3D components will necessitate the development of toolpath planning within each layer. These aspects represent our ongoing research efforts, which are part of the broader and exciting direction initiated by this study.

CRedit authorship contribution statement

Kai Wu: Writing – original draft, Software, Methodology, Conceptualization. **Weiming Wang:** Writing – review & editing, Methodology. **Fred van Keulen:** Writing – review & editing, Supervision. **Jun Wu:** Writing – review & editing, Supervision, Methodology, Conceptualization.

Declaration of competing interest

The authors declare that they have no known competing financial interests or personal relationships that could have appeared to influence the work reported in this paper.

Data availability

No data was used for the research described in the article.

Acknowledgments

The authors would like to thank Dr. Can Ayas and Dr. Vibhas Mishra for their valuable suggestions during our discussion. Kai Wu is supported by China Scholarship Council (No. 202006210069). Weiming Wang wishes to thank the National Natural Science Foundation of China (No. 62172073). This work is also partly supported by the Dutch Research Council (NWO), The Netherlands with project number 20382, “Space-time optimization for additive manufacturing”.

Appendix A. Generalized Hooke’s law of orthotropic material

The generalized Hooke’s law of an orthotropic material in the Voigt notation is

$$\sigma_0 = \mathbf{D}_0 \varepsilon_0, \quad (25)$$

where ε_0 and σ_0 denote the stress and strain tensor, respectively. \mathbf{D}_0 represents the elasticity tensor. For plane stress problems with infinitesimal strain, and with the horizontal axis denoted as x and the vertical axis as y , the elasticity tensor is expressed as

$$\mathbf{D}_0 = \frac{1}{1 - \nu_{xy}\nu_{yx}} \begin{bmatrix} E_x & \nu_{yx}E_x & 0 \\ \nu_{xy}E_y & E_y & 0 \\ 0 & 0 & G_{xy}(1 - \nu_{xy}\nu_{yx}) \end{bmatrix}, \quad (26)$$

where E_x and E_y are the Young's modulus along the reference axes, and G_{xy} is the shear modulus. ν_{xy}, ν_{yx} are the Poisson's ratio, satisfying $\nu_{xy}E_y = \nu_{yx}E_x$.

Appendix B. Sensitivity analysis

We focus on the sensitivity of the objective function related to the material anisotropy. For the sensitivities of constraints in various application scenarios of space-time topology optimization, we refer to the work of Wang et al. [77].

The objective function is determined by optimization variables ϕ and μ via two intermediate fields, the density field $\rho = \tilde{\phi}$, and the time field t . The time field, according to Eq. (11), is determined by both the density field ρ and the thermal diffusivity field $\tilde{\mu}$. Re-writing the objective function by

$$\mathbb{f}_0(\rho, \tilde{\mu}) = f_0(\rho, t(\rho, \tilde{\mu})), \quad (27)$$

the sensitivity of the objective function with respect to ρ and $\tilde{\mu}$ are, respectively,

$$\frac{\partial \mathbb{f}_0}{\partial \rho_e} = \frac{\partial f_0}{\partial \rho_e} + \frac{\partial f_0}{\partial t} \frac{\partial t}{\partial \rho_e}, \quad (28)$$

and

$$\frac{\partial \mathbb{f}_0}{\partial \tilde{\mu}_e} = \frac{\partial f_0}{\partial t} \frac{\partial t}{\partial \tilde{\mu}_e}. \quad (29)$$

Sensitivity w.r.t design variable ϕ . The augmented form of the objective function is written as:

$$\mathbb{f}_0 = f_0 + \lambda^\top (\mathbf{b} - \mathbf{K}_T \mathbf{T}), \quad (30)$$

where λ is the vector of Lagrange multipliers. The sensitivity of the objective function in relation to the density is:

$$\begin{aligned} \frac{\partial \mathbb{f}_0}{\partial \rho_e} &= \frac{\partial f_0}{\partial \rho_e} + \frac{\partial f_0}{\partial t} \frac{\partial t}{\partial \rho_e} + \lambda^\top \left(\frac{\partial \mathbf{b}}{\partial \rho_e} - \frac{\partial \mathbf{K}_T}{\partial \rho_e} \mathbf{T} - \mathbf{K}_T \frac{\partial \mathbf{T}}{\partial \rho_e} \right), \\ &= \frac{\partial f_0}{\partial \rho_e} - \frac{\partial f_0}{\partial t} \frac{\partial \mathbf{T}}{\partial \rho_e} + \lambda^\top \left(-\frac{\partial \mathbf{K}_T}{\partial \rho_e} \mathbf{T} - \mathbf{K}_T \frac{\partial \mathbf{T}}{\partial \rho_e} \right), \\ &= \frac{\partial f_0}{\partial \rho_e} - \left(\frac{\partial f_0}{\partial t} + \lambda^\top \mathbf{K}_T \right) \frac{\partial \mathbf{T}}{\partial \rho_e} - \lambda^\top \frac{\partial \mathbf{K}_T}{\partial \rho_e} \mathbf{T}. \end{aligned} \quad (31)$$

By setting the Lagrange multiplier according to the equation:

$$\frac{\partial f_0}{\partial t} + \lambda^\top \mathbf{K}_T = \mathbf{0}, \quad (32)$$

the sensitivity of the objective function is simplified to

$$\frac{\partial \mathbb{f}_0}{\partial \rho_e} = \frac{\partial f_0}{\partial \rho_e} - \lambda^\top \frac{\partial \mathbf{K}_T}{\partial \rho_e} \mathbf{T}. \quad (33)$$

Substantiating the objective function, $f_0 = c_0 + \sum_{j=1}^N w_j c_j$, the first part of the above equation is calculated as

$$\frac{\partial f_0}{\partial \rho_e} = \frac{\partial c_0}{\partial \rho_e} + \sum_{j=1}^N w_j \frac{\partial c_j}{\partial \rho_e}, \quad (34)$$

where the adjoint method should again be used, resulting in

$$\frac{\partial c_0}{\partial \rho_e} = \frac{\partial \mathbf{U}^\top \mathbf{K} \mathbf{U}}{\partial \rho_e} = -\mathbf{U}^\top \frac{\partial \mathbf{K}}{\partial \rho_e} \mathbf{U}, \quad (35)$$

and

$$\begin{aligned} \frac{\partial c_j}{\partial \rho_e} &= \frac{\partial (\mathbf{U}^{(j)})^\top \mathbf{K}^{(j)} \mathbf{U}^{(j)}}{\partial \rho_e}, \\ &= 2(\mathbf{U}^{(j)})^\top \frac{\partial \mathbf{G}^{(j)}}{\partial \rho_e} - (\mathbf{U}^{(j)})^\top \frac{\partial \mathbf{K}^{(j)}}{\partial \rho_e} \mathbf{U}^{(j)}. \end{aligned} \quad (36)$$

Here the external load on intermediate structures $\mathbf{G}^{(j)}$ can be design dependent, e.g., self-weight.

Lastly, by using the chain rule, the sensitivity of the objective function in relation to the optimization variable ϕ can be computed using:

$$\frac{\partial \mathbb{f}_0}{\partial \phi_e} = \sum_{i \in \mathcal{N}_e} \frac{\partial \mathbb{f}_0}{\partial \rho_i} \frac{\partial \rho_i}{\partial \phi_e} + \frac{\partial \mathbb{f}_0}{\partial \tilde{\mu}_i} \frac{\partial \tilde{\mu}_i}{\partial \phi_e}. \quad (37)$$

Sensitivity w.r.t design variable μ . The sensitivity of the objective function in relation to the thermal diffusivity $\tilde{\mu}$ is calculated by using the adjoint method as well:

$$\begin{aligned} \frac{\partial \mathbb{f}_0}{\partial \tilde{\mu}_e} &= \frac{\partial f_0}{\partial t} \frac{\partial t}{\partial \tilde{\mu}_e} + \lambda^\top \left(\frac{\partial \mathbf{b}}{\partial \tilde{\mu}_e} - \frac{\partial \mathbf{K}_T}{\partial \tilde{\mu}_e} \mathbf{T} - \mathbf{K}_T \frac{\partial \mathbf{T}}{\partial \tilde{\mu}_e} \right), \\ &= - \left(\frac{\partial f_0}{\partial t} + \lambda^\top \mathbf{K}_T \right) \frac{\partial \mathbf{T}}{\partial \tilde{\mu}_e} - \lambda^\top \frac{\partial \mathbf{K}_T}{\partial \tilde{\mu}_e} \mathbf{T}. \end{aligned} \quad (38)$$

The sensitivity in relation to the original optimization variable μ is computed using the chain rule:

$$\frac{\partial \mathbb{f}_0}{\partial \mu_e} = \sum_{i \in \mathcal{N}_e} \frac{\partial f_0}{\partial \tilde{\mu}_i} \frac{\partial \tilde{\mu}_i}{\partial \mu_e}. \quad (39)$$

Lagrangian multiplier λ . Eqs. (31) and (38) have the same Lagrange multiplier λ . To solve for λ , we need the derivative of the objective function with regard to the nodal time field:

$$\frac{\partial f_0}{\partial t_i} = \frac{\partial c_0}{\partial t_i} + \sum_{j=1}^N w_j \frac{\partial c_j}{\partial t_i}. \quad (40)$$

Again by using the adjoint method we obtain:

$$\frac{\partial c_0}{\partial t_i} = \frac{\partial \mathbf{U}^\top \mathbf{K} \mathbf{U}}{\partial t_i} = \mathbf{U}^\top \frac{\partial \mathbf{K}}{\partial t_i} \mathbf{U} = \sum_e \mathbf{U}_e^\top \frac{\partial \mathbf{K}_e}{\partial t_i} \mathbf{U}_e, \quad (41)$$

$$\begin{aligned} \frac{\partial c_j}{\partial t_i} &= \frac{\partial (\mathbf{U}^{(j)})^\top \mathbf{K}^{(j)} \mathbf{U}^{(j)}}{\partial t_i}, \\ &= 2(\mathbf{U}^{(j)})^\top \frac{\partial \mathbf{G}^{(j)}}{\partial t_i} - \sum_e (\mathbf{U}_e^{(j)})^\top \frac{\partial \mathbf{K}_e^{(j)}}{\partial t_i} \mathbf{U}_e^{(j)}. \end{aligned} \quad (42)$$

The derivative of the stiffness matrices in relation to t_i is obtained using Eq. (9):

$$\begin{aligned} \frac{\partial \mathbf{K}_e}{\partial t_i} &= \left[\varepsilon + (1 - \varepsilon) \rho_e^p \right] \int_{\Omega_e} \left[\mathbf{B}^\top \frac{\partial \mathbf{R}^\top(\theta_e)}{\partial t_i} \mathbf{D}_0 \mathbf{R}(\theta_e) \mathbf{B} \right. \\ &\quad \left. + \mathbf{B}^\top \mathbf{R}^\top(\theta_e) \mathbf{D}_0 \frac{\partial \mathbf{R}(\theta_e)}{\partial t_i} \mathbf{B} \right] d\Omega_e, \end{aligned} \quad (43)$$

$$\begin{aligned} \frac{\partial \mathbf{K}_e^{(j)}}{\partial t_i} &= (1 - \varepsilon) \frac{\partial (\rho_e^{(j)})^p}{\partial t_i} \int_{\Omega_e} \mathbf{B}^\top \mathbf{R}^\top(\theta_e) \mathbf{D}_0 \mathbf{R}(\theta_e) \mathbf{B} d\Omega_e \\ &\quad + \left[\varepsilon + (1 - \varepsilon) (\rho_e^{(j)})^p \right] \int_{\Omega_e} \left[\mathbf{B}^\top \frac{\partial \mathbf{R}^\top(\theta_e)}{\partial t_i} \mathbf{D}_0 \mathbf{R}(\theta_e) \mathbf{B} \right. \\ &\quad \left. + \mathbf{B}^\top \mathbf{R}^\top(\theta_e) \mathbf{D}_0 \frac{\partial \mathbf{R}(\theta_e)}{\partial t_i} \mathbf{B} \right] d\Omega_e. \end{aligned} \quad (44)$$

The derivative of the rotation matrix $\mathbf{R}(\theta_e)$ with regard to t_i is calculated using the chain rule:

$$\frac{\partial \mathbf{R}(\theta_e)}{\partial t_i} = \frac{\partial \mathbf{R}(\theta_e)}{\partial \theta_e} \frac{\partial \theta_e}{\partial t_i}, \quad (45)$$

$\partial \theta_e / \partial t_i$ is non-zero only if node i belongs to element e . From Eq. (6) we get

$$\frac{\partial \theta_e}{\partial t_i} = \frac{\left(\sum_{j \in e} \frac{\partial N_j}{\partial y} t_j \right) \frac{\partial N_i}{\partial x} - \left(\sum_{j \in e} \frac{\partial N_j}{\partial x} t_j \right) \frac{\partial N_i}{\partial y}}{\left(\sum_{j \in e} \frac{\partial N_j}{\partial x} t_j \right)^2 + \left(\sum_{j \in e} \frac{\partial N_j}{\partial y} t_j \right)^2}. \quad (46)$$

References

- [1] Sigmund O, Maute K. Topology optimization approaches. *Struct Multidiscip Optim* 2013;48(6):1031–55.
- [2] Van Dijk NP, Maute K, Langelaar M, Van Keulen F. Level-set methods for structural topology optimization: a review. *Struct Multidiscip Optim* 2013;48(3):437–72.
- [3] Wu Y, Fang J, Wu C, Li C, Sun G, Li Q. Additively manufactured materials and structures: A state-of-the-art review on their mechanical characteristics and energy absorption. *Int J Mech Sci* 2023;246:108102.
- [4] Suárez A, Veiga F, Bhujangrao T, Aldalur E. Study of the mechanical behavior of topologically optimized arc wire direct energy deposition aerospace fixtures. *J Mater Eng Perform* 2022.
- [5] Veiga F, Suárez A, Aldalur E, Goenaga I, Amondarain J. Wire arc additive manufacturing process for topologically optimized aeronautical fixtures. *3D Print Addit Manuf* 2023;10(1):23–33.

- [6] Langelaar M. Topology optimization of 3D self-supporting structures for additive manufacturing. *Addit Manuf* 2016;12:60–70.
- [7] Langelaar M. An additive manufacturing filter for topology optimization of print-ready designs. *Struct Multidiscip Optim* 2017;55(3):871–83.
- [8] van de Ven E, Maas R, Ayas C, Langelaar M, van Keulen F. Continuous front propagation-based overhang control for topology optimization with additive manufacturing. *Struct Multidiscip Optim* 2018;57(5):2075–91.
- [9] Ranjan R, Ayas C, Langelaar M, Keulen FV. Controlling local overheating in topology optimization for additive manufacturing. *Struct Multidiscip Optim* 2022;65(6).
- [10] Wu J, Wang CC, Zhang X, Westermann R. Self-supporting rhombic infill structures for additive manufacturing. *Comput Aided Des* 2016;80:32–42.
- [11] Kuo Y-H, Cheng C-C, Lin Y-S, San C-H. Support structure design in additive manufacturing based on topology optimization. *Struct Multidiscip Optim* 2018;57(1):183–95.
- [12] Allaire G, Jakabčín L. Taking into account thermal residual stresses in topology optimization of structures built by additive manufacturing. *Math Models Methods Appl Sci* 2018;28(12):2313–66.
- [13] Xu S, Liu J, Ma Y. Residual stress constrained self-support topology optimization for metal additive manufacturing. *Comput Methods Appl Mech Engrg* 2022;389:114380.
- [14] Liu J, Gaynor AT, Chen S, Kang Z, Suresh K, Takezawa A, et al. Current and future trends in topology optimization for additive manufacturing. *Struct Multidiscip Optim* 2018;57(6):2457–83.
- [15] Zhu J, Zhou H, Wang C, Zhou L, Yuan S, Zhang W. A review of topology optimization for additive manufacturing: Status and challenges. *Chin J Aeronaut* 2021;34(1):91–110.
- [16] Bayat M, Zinovieva O, Ferrari F, Ayas C, Langelaar M, Spangenberg J, et al. Holistic computational design within additive manufacturing through topology optimization combined with multiphysics multi-scale materials and process modelling. *Prog Mater Sci* 2023;138:101129.
- [17] Williams SW, Martina F, Addison AC, Ding J, Pardal G, Colegrove P. Wire+ arc additive manufacturing. *Mater Sci Technol* 2016;32(7):641–7.
- [18] Jafari D, Vaneker THJ, Gibson I. Wire and arc additive manufacturing: Opportunities and challenges to control the quality and accuracy of manufactured parts. *Mater Des* 2021;109471.
- [19] Abe T, Sasahara H. Layer geometry control for the fabrication of lattice structures by wire and arc additive manufacturing. *Addit Manuf* 2019;28:639–48.
- [20] Langelaar M. Combined optimization of part topology, support structure layout and build orientation for additive manufacturing. *Struct Multidiscip Optim* 2018;57(5):1985–2004.
- [21] Chandrasekhar A, Kumar T, Suresh K. Build optimization of fiber-reinforced additively manufactured components. *Struct Multidiscip Optim* 2020;61(1):77–90.
- [22] Li S, Yuan S, Zhu J, Wang C, Li J, Zhang W. Additive manufacturing-driven design optimization: Building direction and structural topology. *Addit Manuf* 2020;36:101406.
- [23] Wang C, Qian X. Simultaneous optimization of build orientation and topology for additive manufacturing. *Addit Manuf* 2020;34:101246.
- [24] Bruggi M, Laghi V, Trombetti T. Simultaneous design of the topology and the build orientation of wire-and-arc additively manufactured structural elements. *Comput Struct* 2021;242:106370.
- [25] Olesen ArM, Hermansen SM, Lund E. Simultaneous optimization of topology and print orientation for transversely isotropic fatigue. *Struct Multidiscip Optim* 2021;64(3):1041–62.
- [26] Kallai Z, Dammann M, Schueppstuhl T. Operation and experimental evaluation of a 12-axis robot-based setup used for 3D-printing. In: *ISR 2020; 52th international symposium on robotics*. 2020, p. 1–9.
- [27] Dai C, Wang CCL, Wu C, Lefebvre S, Fang G, Liu Y-J. Support-free volume printing by multi-axis motion. *ACM Trans Graph* 2018;37(4):134:1–134:14.
- [28] Fang G, Zhang T, Zhong S, Chen X, Zhong Z, Wang CCL. Reinforced FDM: multi-axis filament alignment with controlled anisotropic strength. *ACM Trans Graph* 2020;39(6):1–15.
- [29] Tang P, Zhao X, Shi H, Hu B, Ding J, Yang B, Xu W. A review of multi-axis additive manufacturing: potential, opportunity and challenge. *Addit Manuf* 2024;104075.
- [30] Wang W, van Keulen F, Wu J. Fabrication sequence optimization for minimizing distortion in multi-axis additive manufacturing. *Comput Methods Appl Mech Engrg* 2023;406:115899.
- [31] Amir O, Mass Y. Topology optimization for staged construction. *Struct Multidiscip Optim* 2018;57(4):1679–94.
- [32] Bruggi M, Parolini N, Regazzoni F, Verani M. Topology optimization with a time-integral cost functional. *Finite Elem Anal Des* 2018;140:11–22.
- [33] Wang W, Munro D, Wang CC, van Keulen F, Wu J. Space-time topology optimization for additive manufacturing. *Struct Multidiscip Optim* 2020;61(1):1–18.
- [34] Boissier M, Allaire G, Tournier C. Concurrent shape optimization of the part and scanning path for powder bed fusion additive manufacturing. *SIAM J Control Optim* 2023;61(2):697–722.
- [35] Li L, Sun Q, Bellehumeur C, Gu P. Composite modeling and analysis for fabrication of FDM prototypes with locally controlled properties. *J Manuf Process* 2002;4(2):129–41.
- [36] Kunze K, Etter T, Grässlin J, Shklover V. Texture, anisotropy in microstructure and mechanical properties of IN738lc alloy processed by selective laser melting (SLM). *Mater Sci Eng A* 2015;620:213–22.
- [37] Zhang P, Liu J, To AC. Role of anisotropic properties on topology optimization of additive manufactured load bearing structures. *Scr Mater* 2017;135:148–52.
- [38] Jiang D, Smith DE. Anisotropic mechanical properties of oriented carbon fiber filled polymer composites produced with fused filament fabrication. *Addit Manuf* 2017;18:84–94.
- [39] Wu B, Pan Z, Ding D, Cuiuri D, Li H, Xu J, et al. A review of the wire arc additive manufacturing of metals: properties, defects and quality improvement. *J Manuf Process* 2018;35:127–39.
- [40] Kok Y, Tan XP, Wang P, Nai MLS, Loh NH, Liu E, et al. Anisotropy and heterogeneity of microstructure and mechanical properties in metal additive manufacturing: A critical review. *Mater Des* 2018;139:565–86.
- [41] Hassel T, Carstensen T. Properties and anisotropy behaviour of a nickel base alloy material produced by robot-based wire and arc additive manufacturing. *Weld World* 2020;64(11):1921–31.
- [42] Bi M, Tran P, Xia L, Ma G, Xie YM. Topology optimization for 3D concrete printing with various manufacturing constraints. *Addit Manuf* 2022;57:102982.
- [43] Zou J, Xia X. Topology optimization for additive manufacturing with strength constraints considering anisotropy. *J Comput Des Eng* 2023;10(2):892–904.
- [44] Wu Y, Yang L. Modeling and analysis of material anisotropy-topology effects of 3D cellular structures fabricated by powder bed fusion additive manufacturing. *Int J Mech Sci* 2021;197:106325.
- [45] Li P, Yvonne J, Wu Y. Improved fracture resistance of 3D-printed elastoplastic structures with respect to their topology and orientation of deposited layers. *Int J Mech Sci* 2022;220:107147.
- [46] Kundu RD, Zhang XS. Additive manufacturing of stiff and strong structures by leveraging printing-induced strength anisotropy in topology optimization. *Addit Manuf* 2023;75:103730.
- [47] Shi Y, Huang Y, Kim IY. Multi-material topology optimization considering both isotropy and anisotropy with fibre orientation optimization. *Eng Optim* 2024;1–25.
- [48] Ray N, Kim IY. Fiber reinforced additive manufacturing: structurally motivated print orientation and sequential topology optimization of anisotropic material. *Rapid Prototyp J* 2024;30(2):305–22.
- [49] Kyvelou P, Slack H, Daskalaki Mountanou D, Wade MA, Britton TB, Buchanan C, et al. Mechanical and microstructural testing of wire and arc additively manufactured sheet material. *Mater Des* 2020;192:108675.
- [50] Mok SH, Bi G, Folkes J, Pashby I, Segal J. Deposition of Ti–6Al–4V using a high power diode laser and wire, Part II: Investigation on the mechanical properties. *Surf Coat Technol* 2008;202(19):4613–9.
- [51] Mishra V, Ayas C, Langelaar M, Keulen F. Simultaneous topology and deposition direction optimization for wire and arc additive manufacturing. *Manuf Lett* 2021;(31):45–51.
- [52] Ramonell C, Chacón R. On the topological optimization of horizontal links in eccentrically braced frames. *J Constr Steel Res* 2021;185:106887.
- [53] Zhou K, Li X. Topology optimization of structures under multiple load cases using a fiber-reinforced composite material model. *Comput Mech* 2006;38(2):163–70.
- [54] Zhou K, Li X. Topology optimization for minimum compliance under multiple loads based on continuous distribution of members. *Struct Multidiscip Optim* 2008;37(1):49–56.
- [55] Sørensen SN, Lund E. Topology and thickness optimization of laminated composites including manufacturing constraints. *Struct Multidiscip Optim* 2013;48(2):249–65.
- [56] Qiu Z, Li Q, Luo Y, Liu S. Concurrent topology and fiber orientation optimization method for fiber-reinforced composites based on composite additive manufacturing. *Comput Methods Appl Mech Engrg* 2022;395:114962.
- [57] Szederkenyi B, Kovacs NK, Czigan T. A comprehensive review of fiber-reinforced topology optimization for advanced polymer composites produced by automated manufacturing. *Adv Ind Eng Polym Res* 2024.
- [58] Pedersen P. On optimal orientation of orthotropic materials. *Struct Optim* 1989;1(2):101–6.
- [59] Pedersen P. Bounds on elastic energy in solids of orthotropic materials. *Struct Optim* 1990;2(1):55–63.
- [60] Suzuki K, Kikuchi N. A homogenization method for shape and topology optimization. *Comput Methods Appl Mech Engrg* 1991;93(3):291–318.
- [61] Díaz AR, Bendsoe MP. Shape optimization of structures for multiple loading conditions using a homogenization method. *Struct Optim* 1992;4(1):17–22.
- [62] Cheng HC, Kikuchi N, Ma ZD. An improved approach for determining the optimal orientation of orthotropic material. *Struct Optim* 1994;8(2–3):101–12.
- [63] Gea HC, Luo JH. On the stress-based and strain-based methods for predicting optimal orientation of orthotropic materials. *Struct Multidiscip Optim* 2004;26(3–4):229–34.
- [64] Safonov AA. 3D topology optimization of continuous fiber-reinforced structures via natural evolution method. *Compos Struct* 2019;215:289–97.

- [65] Eckrich M, Arrabiyeh PA, Dlugaj AM, May D. An anisotropic topology optimization procedure for continuous fiber reinforced polymer structures with biaxial fiber layout for improved intersection point design. *Compos Struct* 2024;337:118064.
- [66] Jiang D, Hoglund R, Smith D. Continuous fiber angle topology optimization for polymer composite deposition additive manufacturing applications. *Fibers* 2019;7(2):14.
- [67] Jantos DR, Hackl K, Junker P. Topology optimization with anisotropic materials, including a filter to smooth fiber pathways. *Struct Multidiscip Optim* 2020;61(5):2135–54.
- [68] Nomura T, Dede EM, Lee J, Yamasaki S, Matsumori T, Kawamoto A, et al. General topology optimization method with continuous and discrete orientation design using isoparametric projection. *Internat J Numer Methods Engrg* 2015;101(8):571–605.
- [69] Lee J, Kim D, Nomura T, Dede EM, Yoo J. Topology optimization for continuous and discrete orientation design of functionally graded fiber-reinforced composite structures. *Compos Struct* 2018;201:217–33.
- [70] Schmidt M-P, Couret L, Gout C, Pedersen CBW. Structural topology optimization with smoothly varying fiber orientations. *Struct Multidiscip Optim* 2020;62(6):3105–26.
- [71] Liu J, Yu H. Concurrent deposition path planning and structural topology optimization for additive manufacturing. *Rapid Prototyp J* 2017;23(5):930–42.
- [72] Chen Q, Liu J, Liang X, To AC. A level-set based continuous scanning path optimization method for reducing residual stress and deformation in metal additive manufacturing. *Comput Methods Appl Mech Engrg* 2020;360:112719.
- [73] Fernandez F, Compel WS, Lewicki JP, Tortorelli DA. Optimal design of fiber reinforced composite structures and their direct ink write fabrication. *Comput Methods Appl Mech Engrg* 2019;353:277–307.
- [74] Xu Y, Feng Z, Gao Y, Wu C, Fang J, Sun G, et al. Topology optimization for additive manufacturing of CFRP structures. *Int J Mech Sci* 2024;269:108967.
- [75] Ichihara N, Ueda M. 3D-printed high-toughness composite structures by anisotropic topology optimization. *Composites B* 2023;253:110572.
- [76] Eckrich M, Arrabiyeh PA, Dlugaj AM, May D. Structural topology optimization and path planning for composites manufactured by fiber placement technologies. *Compos Struct* 2022;289:115488.
- [77] Wang W, Wu K, van Keulen F, Wu J. Regularization in space–time topology optimization for additive manufacturing. *Comput Methods Appl Mech Engrg* 2024;431:117202.
- [78] Sigmund O, Petersson J. Numerical instabilities in topology optimization: A survey on procedures dealing with checkerboards, mesh-dependencies and local minima. *Struct Optim* 1998;16(1):68–75.
- [79] Bruns TE, Tortorelli DA. Topology optimization of non-linear elastic structures and compliant mechanisms. *Comput Methods Appl Mech Engrg* 2001;190(26–27):3443–59.
- [80] Bourdin B. Filters in topology optimization. *Internat J Numer Methods Engrg* 2001;50(9):2143–58.
- [81] Sigmund O. Morphology-based black and white filters for topology optimization. *Struct Multidiscip Optim* 2007;33(4–5):401–24.
- [82] Wang F, Lazarov BS, Sigmund O. On projection methods, convergence and robust formulations in topology optimization. *Struct Multidiscip Optim* 2011;43(6):767–84.
- [83] Svanberg K. The method of moving asymptotes—a new method for structural optimization. *Int J Numer Methods Eng* 1987;24(2):359–73.